Препринти Інституту фізики конденсованих систем НАН України розповсюджуються серед наукових та інформаційних установ. Вони також доступні по електронній комп'ютерній мережі на WWW-сервері інституту за адресою http://www.icmp.lviv.ua/

The preprints of the Institute for Condensed Matter Physics of the National Academy of Sciences of Ukraine are distributed to scientific and informational institutions. They also are available by computer network from Institute's WWW server (http://www.icmp.lviv.ua/)

Степан Петрович Глушак
Юрый Володимирович Калюжний
Пітер Каммінгс

Фазова рівновага у полідисперсній атермальній полімерно-колоїдній суміші

Роботу отримано 20 лютого 2008 р.

Затверджено до друку Вченою радою ІФКС НАН України

Рекомендовано до друку семінаром відділу теорії нерівноважних процесів

Виготовлено при ІФКС НАН України

Національна академія наук України

ІНСТИТУТ ФІЗИКИ КОНДЕНСОВАНИХ СИСТЕМ

ICMP–08–02E

S. P. Hlushak, Yu. V. Kalyuzhnyi, and P. T. Cummings

PHASE COEXISTENCE IN POLYDISPERSE ATHERMAL POLYMER-COLLOIDAL MIXTURE

ЛЬВІВ

УДК: 532; 532.74; 532.772

PACS: 05.70.Ce; 61.20.Gy; 64.75.Va; 64.75.Xc; 82.70.Dd

Фазова рівновага у полідисперсній атермальній полімерно-колоїдній суміші

С.П. Глушак, Ю.В. Калюжний, П.Т. Каммінгс

Анотація. Розроблена раніше теоретична схема використана для обрахунку повної фазової діаграми полідисперсної атермальної колоїдно-полімерної суміші з полідисперсністю полімерної та колоїдної підсистем. Отримані теоретичні результати в граничному випадку бідіспресної колоїдно-полімерної суміші порівнюються з результатами комп'ютерної симуляції. Представлено криві хмари, тіні, критичні бінодалі та функції розподілу співіснуючих фаз, а також проаналізовано вплив на них ефектів полідисперсності. Виявлено, що полідисперсність розширює область фазової нестабільності, зсуваючи критичну точку в сторону менших значень тиску та густини. При великих тисках полідисперсність призводить до появи сильного фракціонування при якому великі колоїдні частинки відокремлюються у розріджену фазу тіні а довгі полімери в густу фазу тіні.

Phase coexistence in polydisperse athermal polymer-colloidal mixture

S. P. Hlushak, Yu. V. Kalyuzhnyi, and P. T. Cummings

Abstract. A theoretical scheme developed earlier is used to calculate the full phase diagram of polydisperse athermal polymer-colloidal mixture with polydispersity in both colloidal and polymeric components. In the limiting case of bidisperse polymer-colloidal mixture theoretical results are compared against computer simulation results. We present the cloud and shadow curves, critical binodals and distribution functions of the coexisting phases and discuss the effects of polydispersity on their behavior. According to our analysis polydispersity extends the region of the phase instability, shifting the critical point to the lower values of the pressure and density. For the high values of the pressure polydispersity causes strong fractionation effects with the large size colloidal particles preferring the low-density shadow phase and long chain length polymeric particles preferring to be in the high-density shadow phase.

1. Introduction

In this paper we continue our study of the phase behavior of athermal polydisperse polymer-colloidal mixtures. In the previous paper [1] we propose a theoretical scheme for the calculation of the full phase diagram (including cloud and shadow curves, binodals and distribution functions of the coexisting phases) for polydisperse athermal polymer-colloidal mixtures with polydispersity in both polymeric and colloidal components. The scheme combines thermodynamic perturbation theory (TPT) for associating fluids [2] and recently developed method used to determine the phase diagram of polydisperse spherical shape colloidal fluids [3]. To illustrate the scheme the full phase diagram for the mixture with polydispersity in the size of the hard-sphere colloidal particles was presented.

Since the pioneering work of Asakura and Oosawa [4, 5] substantial amount of efforts have been focused on the development of the theoretical methods describing the phase behavior of the athermal colloid-polymer mixtures (see Refs. [6–8] and references therein). In the vast majority of the theories developed so far interaction between polymers is either ignored or treated using approximations different from those assumed to describe polymer-colloid and colloid-colloid interactions. This feature imposes certain restrictions on the possibilities of the theory, for example the theories, which ignore polymer-polymer interactions are restricted to the mixtures of short polymers and large colloidal particles (ideal polymer limit). In the frames of the TPT both colloidal and polymeric components are treated on an equal footing. Recently TPT was used to describe the phase behavior of bidisperse polymer-colloidal mixture [8] and polydisperse polymer-colloidal mixture with polydispersity in the polymer chain length [9]. In the latter studies polymers were modeled as a flexible chains of tangentially bonded hard-sphere monomers and colloidal particles were represented as a hard spheres. Effects of polydispersity on the phase behaviour of polymer-colloid mixture were also studied using Asakura and Oosawa level of modelling, i.e. ignoring interactions between polymers [18, 19]. The authors considered influence of only colloid and only polymer polydispersities.

In this study we present and discuss results for the phase behavior of the polymer-colloidal mixture with polydispersity in both components. In our calculations we have used different theories to describe the properties of the reference system, which include Boublik-Mansoori-Carnahan-Starling-Leland [10,11] (BMCSL), Viduna-Smith [12] (VS) and new generalized Carnahan-Starling [13] (NGCS) hard-sphere equations of state

(EOS). To qualify the accuracy of the TPT predictions we compare our results for bidisperse asymmetric hard-sphere mixture and for bidisperse polymer-colloidal mixture with corresponding computer simulation results [14, 15].

2. The model

We consider a polydisperse mixture of hard-sphere flexible chain particles represented by m tangentially bonded hard spheres of diameter σ. In the following we will distinguish between $p-$type of the particles (polymers) and $c-$type of the particles (colloids). Thus the species of each particle is characterized by the set of three variables (a, m, σ) with a denoting the type of the particle (either p or c), $m = 1, 2, ..., \infty$ and $0 \leq \sigma < \infty$. The number density of the $a-$type of the particles is ρ_a and the overall number density ρ is $\rho = \rho_p + \rho_c$. The species variables a, m and σ are distributed according to the distribution function $F_a(m, \sigma)$, which is positive and satisfies the following normalizing conditions

$$\sum_a \sum_m \int d\sigma \; F_a(m, \sigma) = 1. \tag{2.1}$$

Further we put $F_a(m, \sigma) = \alpha_a f_a(m, \sigma)$, where α_a denote the fraction of the $a-$type of the particles

$$\alpha_a = \sum_m \int d\sigma \; F_a(m, \sigma); \tag{2.2}$$

obviously, $\alpha_p + \alpha_c = 1$, and partial distribution functions $f_a(m, \sigma)$ are normalized.

3. Thermodynamical properties

Thermodynamical properties of the model at hand are calculated using TPT of Wertheim [2, 16]. According to TPT Helmholtz free energy of the system A is represented by the sum of three terms

$$A = A_{id} + A_{hs} + A_{ch}, \tag{3.1}$$

where A_{id} is the ideal gas term

$$\frac{A_{id}}{VkT} = \sum_a \rho_a \sum_m \int d\sigma \; F_a(m, \sigma) \left\{ \ln \left[\rho_a F_a(m, \sigma) \right] - 1 \right\}, \tag{3.2}$$

A_{hs} is the hard-sphere term, for which three different expressions have been utilized: BMCSL expression [10, 11]

$$\frac{A_{hs}^{BMCSL}}{VkT} = \frac{6}{\pi} \left[\left(\frac{\zeta_2^3}{\zeta_3^2} - \zeta_0 \right) \ln \Delta + \frac{3\zeta_1\zeta_2}{\Delta} + \frac{\zeta_2^3}{\zeta_3 \Delta^2} \right], \tag{3.3}$$

VS expression, obtained by integrating corresponding pressure expression [12]

$$\begin{aligned} \frac{A_{hs}^{VS}}{VkT} &= \frac{6}{\pi} \left[\left(\frac{\zeta_2}{6\zeta_3^2} \left(13\zeta_1\zeta_3 + 47\zeta_2^2 \right) - \zeta_0 \right) \ln \Delta + \frac{\zeta_2}{2\Delta\zeta_3} \left(7\zeta_1\zeta_3 + 9\zeta_2^2 \right) \right. \\ &\left. + \left(\frac{5\zeta_2}{3\zeta_3} + \frac{\zeta_2}{6\Delta^2} \right) \left(\zeta_1\zeta_3 + 2\zeta_2^2 \right) + \frac{\zeta_2}{12} \left(5\zeta_1\zeta_3 + 7\zeta_2^2 \right) \right], \end{aligned} \tag{3.4}$$

and NGCS expression, which follows from the EOS, proposed by Hansen-Goos and Roth [13]

$$\frac{A_{hs}^{NGCS}}{VkT} = \frac{6}{\pi} \left[\left(\frac{\zeta_1\zeta_2}{\zeta_3} - \frac{\zeta_2^3}{\zeta_3^2} - \zeta_0 \right) \ln \Delta - \frac{\zeta_2^3}{\zeta_3} + \frac{4\zeta_1\zeta_2}{\Delta} + \frac{\zeta_2^3}{\Delta^2\zeta_3} \right], \tag{3.5}$$

and finally, A_{ch} is the term describing formation of the chains

$$\frac{A_{ch}}{VkT} = \rho \sum_a \sum_m (1 - m) \int d\sigma \; F_a(m, \sigma) \ln g_{aa}^{(hs)}(\sigma). \tag{3.6}$$

Here V is the system volume, k is the Boltzmann constant, T is the temperature, $\zeta_0, \zeta_1, \zeta_2, \zeta_3$ are the distribution function moments

$$\zeta_n = \frac{\pi}{6} \rho \sum_a \sum_m m \int d\sigma \; F_a(m, \sigma) \sigma^n, \qquad n = 0, 1, 2, 3; \tag{3.7}$$

$\Delta = 1 - \zeta_3$, $g_{aa}^{(hs)}(\sigma)$ is the hard-sphere radial distribution function (RDF) contact value

$$g_{aa}^{(hs)}(\sigma) = \frac{1}{\Delta} \left(1 + \frac{3}{2}\sigma \frac{\zeta_2}{\Delta} + \frac{1}{2}\sigma^2 \frac{\zeta_2^2}{\Delta^2} \right). \tag{3.8}$$

In (3.8) BMCSL expression for $g_{aa}^{(hs)}(\sigma)$ have been utilized. In a mixture of small and big hard spheres this expression is very accurate in reproducing the contact values of the RDF between small spheres, but fails to accurately predict contact values between big spheres in a sea of small spheres. Thus, in the protein limit (polymer segments are much larger than colloids) expression (3.8) has to be substituted by more accurate

expression. In the present paper we restrict ourselves to the case of the polymer segments much smaller than colloids ($q = \sigma_p/\sigma_c = 0.06$); thus our choice for the RDF contact value (3.8) is justified.

All the rest of the thermodynamical properties can be obtained from Helmholtz free energy using the standard thermodynamical relations. Differentiating Helmholtz free energy with respect to the volume we get the following expression for the pressure:

$$\beta P = \rho + \beta P_{hs} + \beta P_{ch}, \tag{3.9}$$

where $\beta = 1/kT$

$$\beta P_{ch} = \frac{1}{\Delta}\left(\zeta_3\Omega + \zeta_2\Psi\right), \tag{3.10}$$

and for the three different choices of hard-sphere Helmholtz free energy expressions (3.3)-(3.5) we have:

$$\beta P_{hs}^{BMCSL} = \frac{6}{\pi\Delta}\left\{\zeta_0 + \frac{\zeta_2}{\Delta}\left[3\zeta_1 + \frac{\zeta_2^2}{\Delta}\left(2+\Delta\right)\right]\right\}, \tag{3.11}$$

$$\beta P_{hs}^{VS} = \frac{6}{\pi\Delta}\left\{\left(\zeta_0 + 3\zeta_1\zeta_2\right) + \frac{\left(3 - \zeta_3 + \frac{1}{2}\zeta_3^2\right)\zeta_2\left(\zeta_1\zeta_3 + \zeta_2^2\right)}{\Delta} + \frac{2\left(2 - \zeta_3 - \frac{1}{2}\zeta_3^2\right)\zeta_2\zeta_3\left(\zeta_1\zeta_3 + 2\zeta_2^2\right)}{3\Delta^2}\right\} \tag{3.12}$$

and

$$\beta P_{hs}^{NGCS} = \frac{6}{\pi\Delta}\left\{\left(\zeta_0 + \zeta_2^3\right) + \frac{\zeta_1\zeta_2}{\Delta}\left(3 + \zeta_3^2\right) + \frac{2\zeta_2^3}{\Delta^2}\right\}. \tag{3.13}$$

Here

$$\Omega = \rho\sum_a\sum_m (1-m)\int d\sigma\ F_a(m,\sigma)\Omega(\sigma), \tag{3.14}$$

$$\Psi = \rho\sum_a\sum_m (1-m)\int d\sigma\ F_a(m,\sigma)\Psi(\sigma), \tag{3.15}$$

$$\Omega(\sigma) = \frac{\Delta^2 + 3\sigma\zeta_2\left(\Delta + \frac{1}{2}\sigma\zeta_2\right)}{\Delta^2 + \frac{3}{2}\sigma\zeta_2\left(\Delta + \frac{1}{3}\sigma\zeta_2\right)}, \tag{3.16}$$

$$\Psi(\sigma) = \frac{\frac{3}{2}\sigma\Delta\left(\Delta + \frac{2}{3}\sigma\zeta_2\right)}{\Delta^2 + \frac{3}{2}\sigma\zeta_2\left(\Delta + \frac{1}{3}\sigma\zeta_2\right)}. \tag{3.17}$$

Expression for the chemical potential is obtained as a functional derivative of Helmholtz free energy A/V with respect to the function $\rho_a(m,\sigma) = \rho_a F_a(m,\sigma)$:

$$\mu_a(m,\sigma) = \ln\left[\rho_a F(m,\sigma)\right] + \mu_{a,hs}(m,\sigma) + \mu_{a,ch}(m,\sigma), \tag{3.18}$$

where

$$\beta\mu_{a,ch}(m,\sigma) = (1-m)\ln g_{aa}(\sigma) + \frac{\pi}{6}\frac{m\sigma^2}{\Delta}\left(\Omega\sigma + \Psi\right) \tag{3.19}$$

and for $\mu_{a,hs}$ we have:

$$\begin{aligned}\beta\mu_{a,hs}^{BMCSL}(m,\sigma) = m\Bigg[&\sigma^2\frac{\zeta_2^2}{\zeta_3^2}\left(3 - 2\sigma\frac{\zeta_2}{\zeta_3}\right) - 1\Bigg]\ln\Delta \\ &+\frac{m\sigma}{\Delta}\left\{\sigma^2\left[\zeta_0 - \frac{\zeta_2^3}{\zeta_3^2}\left(\frac{1+\Delta}{\Delta}\right) + \frac{6\zeta_2}{\Delta}\left(\frac{\zeta_1}{2} + \frac{\zeta_2^2}{3\zeta_3\Delta}\right)\right]\right. \\ &\left.+3\zeta_2\left(1 + \frac{\sigma\zeta_2}{\zeta_3\Delta}\right) + 3\sigma\zeta_1\right\},\end{aligned} \tag{3.20}$$

$$\begin{aligned}\beta\mu_{a,hs}^{VS}(m,\sigma) = m\Bigg\{\Bigg[&\frac{13\sigma\left(\zeta_2\zeta_3 + \sigma\zeta_1\zeta_3 - \sigma^2\zeta_1\zeta_2\right)}{6\zeta_3^2} \\ &+\frac{47\sigma^2\zeta_2^2\left(3\zeta_3 - 2\sigma\zeta_2\right)}{6\zeta_3^3} - 1\Bigg]\ln\Delta + \left(\frac{\zeta_2}{6\zeta_3^2}\left(13\zeta_1\zeta_3 + 47\zeta_2^2\right) - \zeta_0\right)\frac{\sigma^3}{\Delta} \\ &+\frac{\sigma}{2\Delta^2}\left(7\left(\sigma\zeta_1\Delta + \zeta_2\Delta - \sigma^2\zeta_1\zeta_2\right) + \frac{9\zeta_2^2\sigma}{\zeta_3^2}\left(3\Delta\zeta_3 + \sigma\zeta_3\zeta_3 - \Delta\zeta_2\sigma\right)\right) \\ &+\sigma\left(\left(\frac{5\sigma}{3\zeta_3^2}\left(\zeta_3 - \zeta_2\sigma\right) + \frac{\sigma}{6\Delta^3}\left(\Delta + 2\zeta_2\sigma\right)\right)\left(\zeta_1\zeta_3 + 2\zeta_2^2\right)\right. \\ &\left.+\left(\frac{5\zeta_2}{3\zeta_3} + \frac{\zeta_2}{6\Delta^2}\right)\left(\zeta_3 + \sigma^2\zeta_1 + 4\sigma\zeta_2\right)\right) \\ &+\frac{\sigma}{12}\left(5\left(\zeta_2\zeta_3 + \sigma\zeta_1\zeta_3 + \sigma^2\zeta_1\zeta_2\right) + 21\sigma\zeta_2^2\right)\Bigg\},\end{aligned} \tag{3.21}$$

$$\begin{aligned}\beta\mu_{a,hs}^{NGCS}(m,\sigma) = m\Bigg[&\left(\frac{2\zeta_2^3}{\zeta_3^3} - \frac{\zeta_1\zeta_2}{\zeta_3^2}\right)\sigma^3 + \left(\frac{\zeta_1}{\zeta_2} - \frac{3\zeta_2^2}{\zeta_3^2}\right)\sigma^2 \\ &+\frac{\zeta_2}{\zeta_3}\sigma - 1\Bigg]\ln\Delta + \frac{m\sigma}{\Delta}\left\{\left(\sigma^2\left(\zeta_2^3 - \zeta_1\zeta_2 + \zeta_0\right) + 4\zeta_1\sigma + 4\zeta_2\right)\right. \\ &\left.+\frac{\sigma\zeta_2\left(4\sigma\zeta_1 + 3\zeta_2\right)}{\Delta} + \frac{2\sigma^2\zeta_2^3}{\Delta^2}\right\} + m\sigma^2\left\{\frac{\left(\sigma\left(\zeta_2^3 - \zeta_1\zeta_1\right) - 3\zeta_2^2\right)}{\zeta_3} + \frac{2\zeta_2^3}{\zeta_3^2}\right\}.\end{aligned} \tag{3.22}$$

One can easily see that thermodynamical properties of the model at hand are defined by the set of a finite number of the distribution function moments, i.e. four regular moments $\zeta_0, \zeta_1, \zeta_2, \zeta_3$ and two generalized moments (Ω, Ψ). Thus polydisperse mixture of the chain particles treated within TPT belong to the class of truncatable free energy models [17]. Since detailed description of the method, which is used to calculate the phase diagram of the model in question is presented in our previous publication [1], we will not describe it here and proceed to the discussion of the numerical results.

4. Results and discussion

To verify the accuracy of hard-sphere EOS discussed above, we calculate the phase diagram for binary asymmetric hard-sphere mixture with size ratio $q = 0.1$. Corresponding binodals together with computer simulation results of Dijkstra et al. [14] are demonstrated in Fig. 1. Note that this fluid-fluid phase coexistence is metastable, since it is preempted by the fluid-solid phase transition. It is well known, that BMCSL EOS doesn't show any phase coexistence for binary hard-sphere mixtures. The other two examined EOS appear to be more accurate and do show the phase coexistence. However, quantitative agreement between theory and simulation is not very good. VS EOS coexistence region is located at too high values of η_c and too low values of η_p. Predictions of NGCS EOS is more accurate and underestimate only packing fraction of the small spheres η_p.

In Fig. 2. we present TPT fluid-fluid binodals for colloid-polymer mixtures with size ratio $q = 0.14142$ and polymer chain length $m = 60$ and $m = 100$. Theoretical predictions are compared with computer simulation results of Chou et al. [15]. In general NGCS TPT appears to be the most accurate. Although BMCSL TPT gives the critical packing fraction of the polymers in good agreement with computer simulation predictions, the corresponding critical value of colloid reduced density $\rho_c\sigma_c^3$ is much too high and in the $\rho_c\sigma_c^3$ vs $\rho_p^{mon.}$ plane, location of the NGCS TPT critical point is in better agreement with location of computer simulation critical point. Here $\rho_p^{mon.}$ denotes reduced monomer density: $\rho_p^{mon.} = m\rho_p\sigma_p^3$.

Next we proceed to the polydisperse version of the model with polydispersity in the hard-sphere colloidal size and polymer chain length. We assume, that hard-sphere size of the polymer chain monomers $\sigma_p$is the same for all chains. Thus, for the distribution functions of the parent

phase $F_a^{(0)}(m,\sigma)$, we have

$$F_p^{(0)}(m,\sigma) = \alpha_p^{(0)}\delta\left(\sigma-\sigma_p\right) f_p^{(0)}\left(m\right), \tag{4.1}$$

$$F_c^{(0)}(m,\sigma) = \alpha_c^{(0)} f_c^{(0)}(\sigma)\delta_{m,1}, \tag{4.2}$$

where for the colloidal diameter distribution $f_c^{(0)}(\sigma)$ and polymer chain length distribution $f_p^{(0)}\left(m\right)$, we have chosen the beta-distributions, given by

$$\begin{aligned} f_c^{(0)}(\sigma) &= B^{-1}(\gamma_c,\nu_c)\left(\frac{\sigma}{\sigma_m}\right)^{\gamma_c-1}\left(1-\frac{\sigma}{\sigma_m}\right)^{\nu_c-1}\theta\left(\sigma_m-\sigma\right), \\ f_p^{(0)}(m) &= B^{-1}(\gamma_p,\nu_p)\left(\frac{m}{m_m}\right)^{\gamma_p-1}\left(1-\frac{m}{m_m}\right)^{\nu_p-1}\theta\left(m_m-m\right), \end{aligned}$$

where $\theta(x)$ is the Heaviside step function, $B(\gamma,\nu)$ is the Beta function and corresponding γ and ν are parameters related to the first and second distribution function moments by

$$\gamma_c = \frac{\sigma_m - \langle\sigma\rangle_c^{(0)}\left(1+D_\sigma^{(0)}\right)}{D_\sigma^{(0)}\sigma_m}, \quad \nu_c = \left(\frac{\sigma_m-\langle\sigma\rangle_c^{(0)}}{\langle\sigma\rangle_c^{(0)}}\right)\gamma_c,$$

$$\gamma_p = \frac{m_m - \langle m\rangle_p^{(0)}\left(1+D_m^{(0)}\right)}{D_m^{(0)}m_m}, \quad \nu_p = \left(\frac{m_m-\langle m\rangle_p^{(0)}}{\langle m\rangle_p^{(0)}}\right)\gamma_p,$$

with moments given by

$$\langle\sigma^n\rangle_c^{(\alpha)} = \int d\sigma\ \sigma^n f_c^{(\alpha)}(\sigma), \quad D_\sigma^{(\alpha)} = \langle\sigma^2\rangle_c^{(\alpha)}/\left(\langle\sigma\rangle_c^{(\alpha)}\right)^2 - 1, \tag{4.3}$$

$$\langle m^n\rangle_p^{(\alpha)} = \sum_m m^n f_p^{(\alpha)}(m), \quad D_m^{(\alpha)} = \langle m^2\rangle_p^{(\alpha)}/\left(\langle m\rangle_p^{(\alpha)}\right)^2 - 1 \tag{4.4}$$

Here and beyond upper index $(\cdots)^{(\alpha)}$ will denote some property of mother phase ($\alpha = 0$) or one of the daughter phases ($\alpha = 1, 2$).

Our results for the phase behavior of the model at hand are shown in Figs. 3-12. We present results obtained using BMCSL and NGCS versions of the TPT. Calculations were carried out for the model parameters chosen to be: $\langle m\rangle_p^{(0)} = 50$, $\langle\sigma\rangle_p^{(0)}/\langle\sigma\rangle_c^{(0)} = 0.06$, $D_\sigma^{(0)} = 0.1$, $D_m^{(0)} = 0.1$, $\sigma_m = 2\langle\sigma\rangle_c^{(0)}$ and $m_m = 100$.

Current approach was not extended to treat solid (crystal) phases, and thus we are not able to predict appearance of solids. But we may

speculate whether discussed here gas-liquid coexistence of system with parameters chosen above is stable with respect to appearance of solid phases by using Fasolo and Sollich [19] results. The authors considered system with polydisperse colloid and monodisperse polymers, and found that for almost monodisperse $\delta = \sqrt{D_\sigma} = 0.01$ colloid subsystem, the minimal polymer-colloid size ratio above which gas-liquid becomes stable is $\xi = 2R_p/\sigma_c \approx 0.32$, while for significantly polydisperse system $\delta = \sqrt{D_\sigma} = 0.1$ the size ratio decreases to $\xi = 2R_p/\sigma_c \approx 0.25$. Here R_p denotes radius of gyration of polymer chain, but in original paper [19] the $2R_p = \sigma_p^{AO}$ was diameter of semi-permeable hard spheres, which modelled polymers. In our case, we have strongly polydisperse system $\delta = \sqrt{D_\sigma} \approx 0.32$, with polymers, when treated as ideal chains, having radius of gyration $R_p = \sigma_p\sqrt{\frac{m}{6}} = 0.06\sqrt{\frac{50}{6}} = 0.173$. Thus, our system has rather big polymer-colloid size ratio $\xi = 2R_p/\sigma_c \approx 0.35$, which, as predicted by the free volume theory [19], should be enough to stabilize gas-liquid coexistence even in monodisperse system. Although, the large polymers and strong polydispersity tend to stabilize gas-liquid coexistence, they cannot fully suppress the appearance of solids, so the crystalline solid phases are expected to appear somewhere at high colloid and low polymer packing fractions.

At a sufficiently low density of the parent phase $\rho^{(0)}$ the mixture is stable as a single phase. As $\rho^{(0)}$ is increased the system will phase separate into two phases: low-density phase and high-density phase. In Figs. 3-6 we show the phase diagrams in a different coordinate frames, i.e. P^* vs ρ^* (Fig. 3), P^* vs α_p (Fig. 4), η vs ρ^* (Fig. 5) and η_p vs η_c (Fig. 6), where $P^* = \beta P(\langle\sigma\rangle_c^{(0)})^3$, $\rho^* = \rho(\langle\sigma\rangle_c^{(0)})^3$, η and η_a are the overall packing fraction and the packing fraction of the $a-$type of the particles, respectively. Figs. 7-10 show the phase diagram in $\langle(\Delta m)^2\rangle_p^{(\alpha)}$, $\langle(\Delta\sigma^*)^2\rangle_c^{(\alpha)}$, $\langle m\rangle_p^{(\alpha)}$ and $\langle\sigma^*\rangle_c^{(\alpha)}$ vs α_p coordinates and are intended to give better understanding of the fractionation effects between coexisting phases. Here the former two quantities represent the variance of chain length m and reduced colloid diameter $\sigma^* = \sigma/\langle\sigma\rangle_c^{(\alpha)}$, i.e. $\Delta m = m - \langle m\rangle_p^{(\alpha)}$ and $\Delta\sigma^* = \sigma^* - \langle\sigma\rangle_c^{(\alpha)}/\langle\sigma\rangle_c^{(0)}$. In all the figures shadow and cloud curves are marked by filled and empty triangle or rectangle points and critical binodals are marked by two filled or two empty circle points. The role of these points is twofold. First, the pairs of points of the same type on the shadow and cloud curves or on the two branches of the binodals mark the points, which are in equilibrium. For these points in Figs. 11 and 12 we present distribution functions of the coexisting phases. Second, these points are used to distinguish the cloud and shadow curves

obtained using either BMCSL TPT (rectangle points) or NGCS TPT (triangle points).

The phase diagrams in Figs. 3-10 include cloud and shadow curves and critical binodals for the two theories. For the sake of comparison in Figs. 3-6 we also present the binodals for bidisperse version of the model with ($D_\sigma^{(0)} = 0$ and $D_m^{(0)} = 0$). Critical binodals were calculated for the constant critical values of the parent phase polymer fractions $\alpha_{p,cr}^{(0)} = 0.7431$ for BMCSL TPT and $\alpha_{p,cr}^{(0)} = 0.6772$ for NGCS TPT. Critical points, which are located on the intersection of the corresponding cloud and shadow curves, are marked by filled circles.

Both versions of the TPT give qualitatively similar results, with NGCS TPT predicting slightly weaker effects due to polydispersity. Since in the case of bidisperse mixture NGCS TPT is more accurate (Fig. 2) it is reasonable to expect that similar holds in the case of polydisperse mixture. Comparison between the bidisperse and polydisperse versions of the mixture shows that in agreement with the previous studies [19,20] polydispersity extends the region of the phase instability, shifting the critical point to the lower values of the pressure and density ($P_{cr,bid}^* = 9.93$, $P_{cr,polyd}^* = 5.127$, $\rho_{cr,bid}^* = 2.08$, $\rho_{cr,polyd}^* = 1.363$) and to slightly lower values of the polymer fraction ($\alpha_{p,cr}^{(bid)} = 0.776$, $\alpha_{p,cr}^{(polyd)} = 0.743$) in the case of the BMCSL TPT. Similar holds in the case of the NGCS TPT, i.e. critical pressure, density and polymer fraction are decreased ($P_{cr,bid}^* = 6.831D$, $P_{cr,polyd}^* = 3.838$, $\rho_{cr,bid}^* = 1.583$, $\rho_{cr,polyd}^* = 1.058$, $\alpha_{p,cr}^{(bid)} = 0.7255$, $\alpha_{p,cr}^{(polyd)} = 0.6772$). Fig. 5 shows that packing fraction of the low-density shadow phase (corresponding shadow curves are marked by empty triangle and empty rectangle points) is higher than that of the high-density shadow phase (the shadow curves are marked by filled triangle and filled rectangle points). This is not surprising, since from Fig. 6 we can see, that the main contribution to resulting packing fraction of the two phases is made by the colloidal particles; their fraction and size is higher in the low-density phase (see Fig. 10). Figs. 9 and 10 show that the low-density shadow phase consist mostly of the big size colloids and small fraction of the short chains, while the high-density shadow phase is formed mainly by the long chains and small fraction of the small size colloids. The low-density branch of the critical binodal contains small fraction of short chains and colloids with the average size $\langle\sigma\rangle_c^{(low)} \approx \langle\sigma\rangle_c^{(0)}$. On the other hand the high-density branch have small fraction of small size colloids and polymers with the average chain length $\langle m\rangle_c^{(high)} \approx \langle m\rangle_c^{(0)}$.

This can be seen in more detail in Figs. 11 and 12, where distribu-

tion functions for the states marked by the points located on the shadow curves and critical binodals (Figs. 3-10) are presented. In Fig. 11 the maximum of the colloidal (polymer) distribution function $f_c(\sigma)$ ($f_p(m)$) of the low-density shadow phase is located at $\sigma \approx 1.8\langle\sigma\rangle_c^{(0)}$ ($m \approx 30$) and in the high-density shadow phase at $\sigma \approx 0.7\langle\sigma\rangle_c^{(0)}$ ($m \approx 63$). Corresponding shifts of the distribution functions maxima of the critical binodal (Fig. 12) are less pronounced. Colloidal distribution function of the low-density branch and polymer distribution function of the high-density branch almost coincide with corresponding distribution function of the mother phase. At the same time low-density maximum of the polymer distribution function and high-density maximum of the colloidal distribution function are slightly shifted towards the lower values of m and σ. These maxima are higher and more narrow in comparison with the maxima of the corresponding distribution functions of the mother phase. This can be deduced also from Figs. 7 and 8, where the variances $\langle(\Delta m)^2\rangle_p^{(\alpha)}$ and $\langle(\Delta\sigma^*)^2\rangle_c^{(\alpha)}$ along the shadow curves and critical binodals are presented as a functions of α_p. According to fig. 7 the variance of the polymer chain length along the shadow curves and binodals is always smaller in comparison with the variance in the mother phase. Similar apply for the variance of the colloidal hard-sphere size at all values of α_p, except small region below its critical value. In these region the pressure of the system takes its minimum values (see Fig. 4). With the pressure increase $\langle(\Delta\sigma^*)^2\rangle_c^{(\alpha)}$ ($\langle(\Delta m)^2\rangle_c^{(\alpha)}$) tends to zero only along the high-density (low-density) branch of the critical binodal. Along the low-density (high-density) branch we have: $\langle(\Delta\sigma^*)^2\rangle_c^{(low)} \approx \langle(\Delta\sigma^*)^2\rangle_c^{(0)}$ ($\langle(\Delta m)^2\rangle_c^{(high)} \approx \langle(\Delta\ m)^2\rangle_c^{(0)}$). At the same time the variances of both quantities along the shadow phase curve decrease (Figs. 4, 7 and 8), approaching zero values. Thus at sufficiently high pressure low-density and high-density shadow phases will be almost monodisperse and composed mostly of the large colloidal particles in the low-density case and mostly of long polymer chains in the high-density case. This effect could be used to extract from polydisperse polymer-colloidal mixture either colloidal or polymeric particles with low degree of polydispersity.

5. Conclusions

In this paper phase behavior of athermal polydisperse polymer-colloidal mixture with polydispersity in both polymeric and colloidal components is studied. For theoretical description we have used three different versions of the TPT for polymers [2,16]. In the first version the reference system, represented by polydisperse hard-sphere mixture, is described using BMCSL EOS [10, 11], in the second version we have used VS EOS [12] and in the third version NGCS EOS [13]. In the case of bidisperse asymmetric hard-sphere mixture the latter two EOS show the existence of the metastable liquid-liquid phase transition. Comparison of the theoretical and computer simulation results for the phase diagrams of bidisperse asymmetric hard-sphere mixture [14] and bidisperse polymer-colloidal mixture [15] demonstrate that NGCS TPT predictions are more accurate then VS TPT and BMCSL TPT predictons. We present the full phase diagram of the mixture (including critical binodals, cloud and shadow curves and distribution functions of the coexisting phases) and discuss the effects of the polydispersity on the phase behavior of the system. According to our analysis polydispersity extends the region of the phase instability, shifting the critical point to the lower values of the pressure and density and to slightly lower values of the polymer fraction. For the high values of the pressure the shadow phase is almost monodisperse with the low-density branch consisting of the large size colloidal particles and high-density branch consisting of the long polymer chain particles.

References

1. Yu. V. Kalyuzhnyi, P. T. Cummings, *Chem. Phys. Lett.* **443**, 243 (2007).
2. M. S. Wertheim, *J. Chem. Phys.* **87** 7323 (1987).
3. L. Bellier-Castella, H. Xu, M. Baus, *J. Chem. Phys.* **113**, 8337 (2000).
4. S. Asakura, F. Oosawa, *J. Chem. Phys.* **22**, 1255 (1954).
5. S. Asakura, F. Oosawa, *J. Polym. Sci.* **33**, 183 (1958).
6. R. Tuinier, J. Rieger, de Kruif C.G., *Adv. Colloid. Interface Sci.* **103**, 1 (2003).
7. M. Fuchs, K. S. Schweizer *J. Phys. (Condens. Matt.)* **14**, R239 (2002).
8. P. Paricaud, S. Varga, G. Jackson G., *J. Chem. Phys.* **118**, 8525 (2003).
9. P. Paricaud, S. Varga, P. T. Cummings, G. Jackson, *Chem. Phys. Lett.* **398**, 489 (2004).
10. T. Boublik, *J. Chem. Phys.* **53**, 471 (1970).
11. G. A. Mansoori, N. F. Carnahan, K. E. Starling, I. W. Leland, *J. Chem. Phys.* **54**, 1523 (971).
12. D. Viduna, W.R. Smith, *Mol. Phys.* **100**, 2903 (2002).

13. H. Hansen-Goos, R. Roth, *J. Chem. Phys.* **124**, 154506 (2006).
14. M. Dijkstra, R. van Roij, and R. Evans, *Phys. Rev. E.* **59**, 5744 (1999).
15. C.-Y. Chou, T.T.M. Vo, A.Z. Panagiotopoulos, M. Roberts, *Physica A* **369**, 275 (2006).
16. W. G. Chapman, G. Jackson, K. E. Gubbins, *Mol. Phys.* **65**, 1057 (1988).
17. P. Sollich, *J. Phys. (Condens. Matt.)* **14**, R79 (2002).
18. M. Fasolo, P. Sollich, *J. Phys. Cond. Matt.* **17**, 797 (2005).
19. M. Fasolo, P. Sollich, *J. Chem. Phys.* **122**, 074904 (2005).
20. R. M. L. Evans, *J. Chem. Phys.* **114**, 1915 (2001).

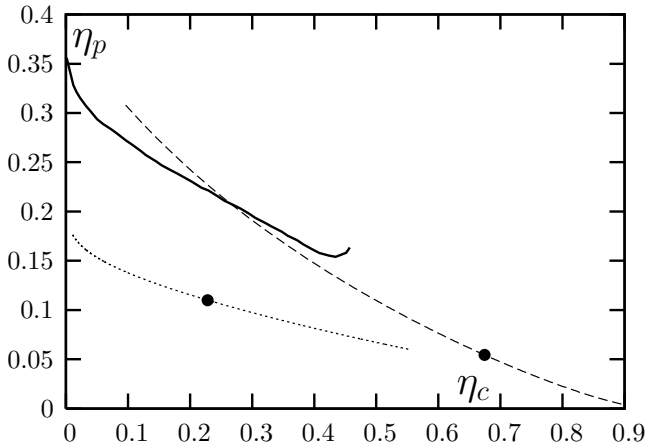

Figure 1. Phase diagram for the two component hard-sphere mixture with the size ratio $q = \sigma_p/\sigma_c = 0.06$ in η_c vs η_p coordinate frames, where η_c and η_p are packing fractions of the big and small spheres, respectively. Thick solid line represents binodal curve due to Dijkstra et al. [14], dashed line represents binodal curve calculated using VS EOS, and dotted line denotes binodal curve predicted using NGCS EOS. Critical points are indicated by the filled circles.

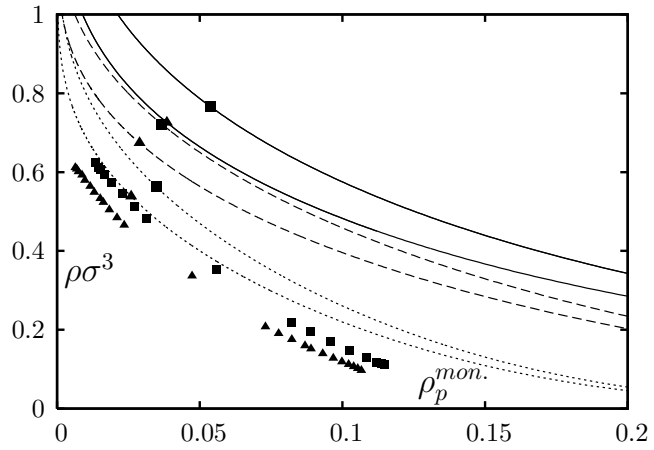

Figure 2. Phase diagram for the bidisperse polymer-colloidal mixture with size ratio $q = \sigma_p/\sigma_c = 0.1414$ in $\rho_c\sigma_c^3$ vs $\rho_p^{mon.}$ coordinate frames, where $\rho_c\sigma_c^3$ is colloidal reduced density and $\rho_p^{mon.}$ is polymer monomer reduced density. Computer simulation results [15] for $m = 60$ and $m = 100$ are represented by filled rectangles and filled triangles, respectively. Corresponding binodals for BMCSL, VS and NGCS versions of the TPT are denoted by the solid, dashed and dotted lines, respectively. Critical points for $m = 60$ and $m = 100$ are indicated by the filled rectangles or filled triangles.

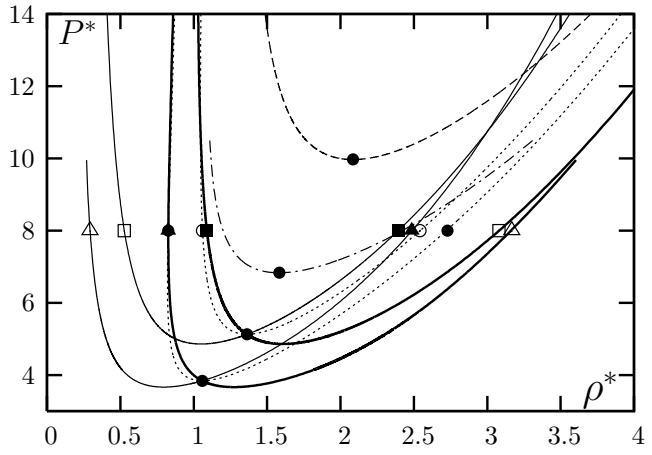

Figure 3. Phase diagram for polydisperse polymer-colloidal mixture in P^* vs ρ coordinate frames. Cloud and shadow curves are represented by thick and thin solid lines, respectively, critical binodal curves with $\alpha_{p,cr}^{(0)} = 0.7431$ (BMCSL TPT) and $\alpha_{p,cr}^{(0)} = 0.6772$ (NGCS TPT) by dotted lines, respectively. Cloud and shadow curves calculated using BMCSL TPT and NGCS TPT are marked by empty and filled rectangle points and empty and filled triangle points, respectively. BMCSL and NGCS critical binodals are marked by empty and filled circle points, respectively. All points are chosen at $P^* = 8$ and pairs of the same points denote the states in equilibrium. Dashed and dashed-dotted lines denote the binodals for the bidisperse version of the model, calculated using BMCSL TPT and NGCS TPT, respectively. Critical points are indicated by filled circles.

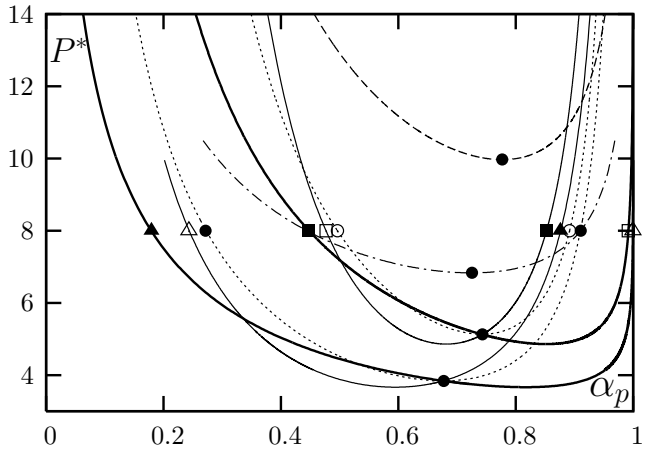

Figure 4. Phase diagram for polydisperse polymer-colloidal mixture in P^* vs α_p coordinate frames. All the notation is the same as in Fig. 3.

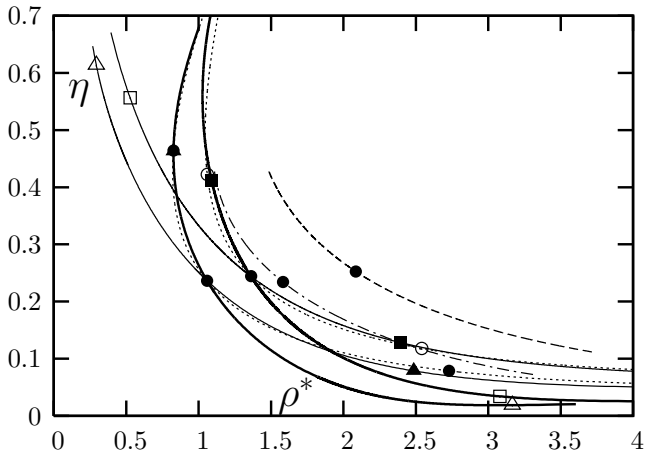

Figure 5. Phase diagram for polydisperse polymer-colloidal mixture in η vs ρ^* coordinate frames. All the notation is the same as in Fig. 3.

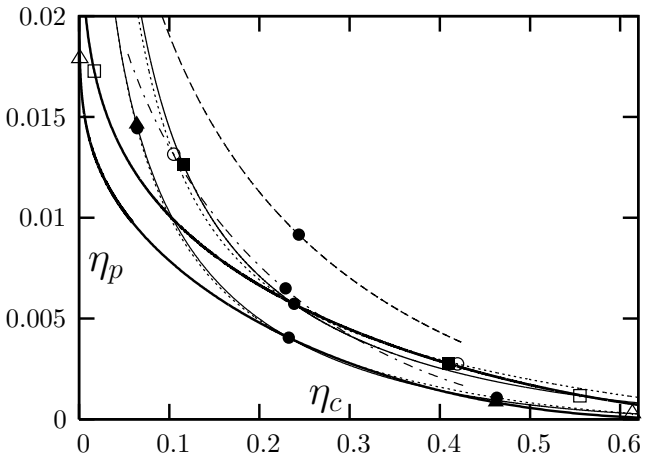

Figure 6. Phase diagram for polydisperse polymer-colloidal mixture in η_p vs η_c coordinate frames, where where η_p is the polymer packing fraction, and η_c is the colloidal packing fraction. All the notation is the same as in Fig. 3.

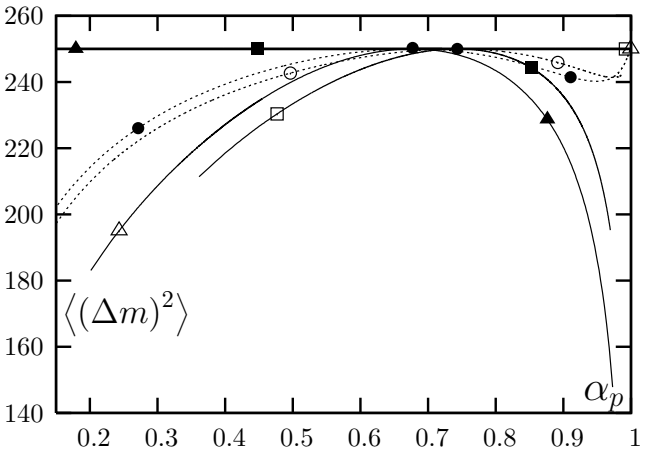

Figure 7. Phase diagram for polydisperse polymer-colloidal mixture in $\langle (\Delta m)^2 \rangle_p^{(\alpha)}$ vs α_p coordinate frames. All the notation is the same as in Fig. 3.

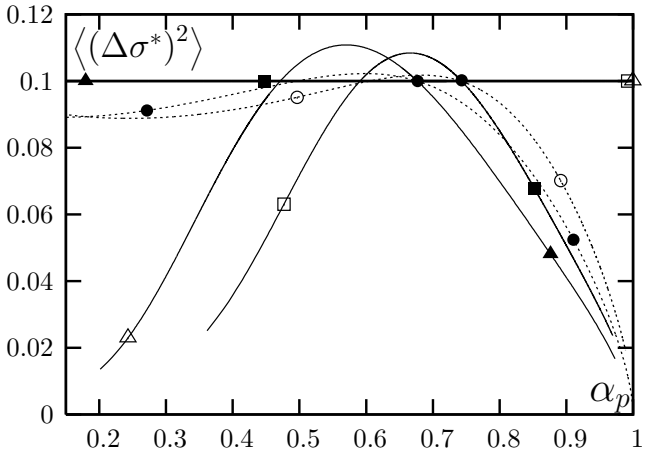

Figure 8. Phase diagram for polydisperse polymer-colloidal mixture in $\langle(\Delta\sigma^*)^2\rangle_c^{(\alpha)}$ vs α_p coordinate frames. All the notation is the same as in Fig. 3.

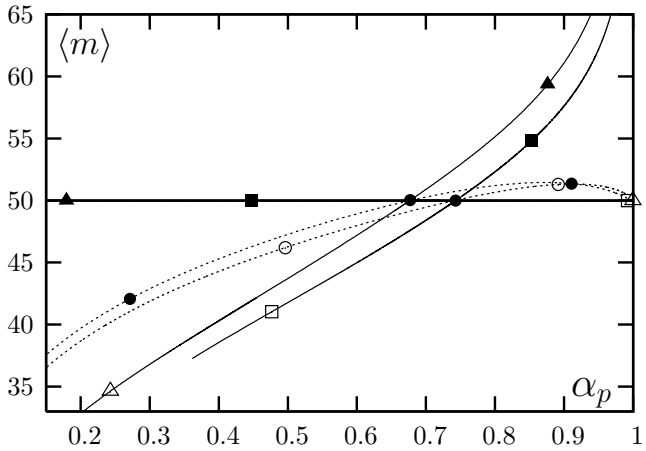

Figure 9. Phase diagram for polydisperse polymer-colloidal mixture in $\langle m\rangle_p^{(\alpha)}$ vs α_p coordinate frames. All the notation is the same as in Fig. 3.

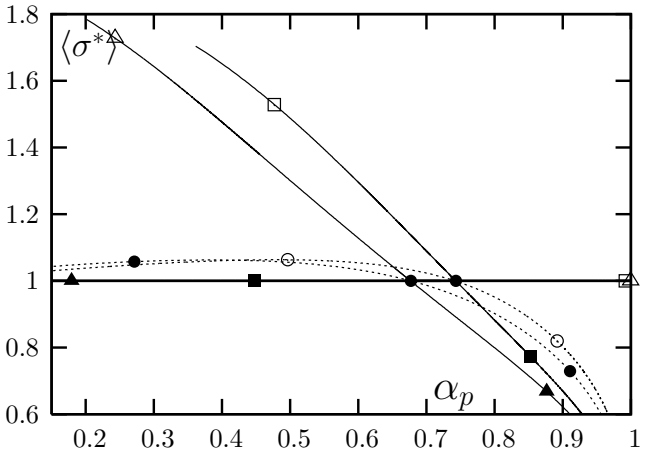

Figure 10. Phase diagram for polydisperse polymer-colloidal mixture in $\langle\sigma^*\rangle_c^{(\alpha)}$ vs α_p coordinate frames. All the notation is the same as in Fig. 3.

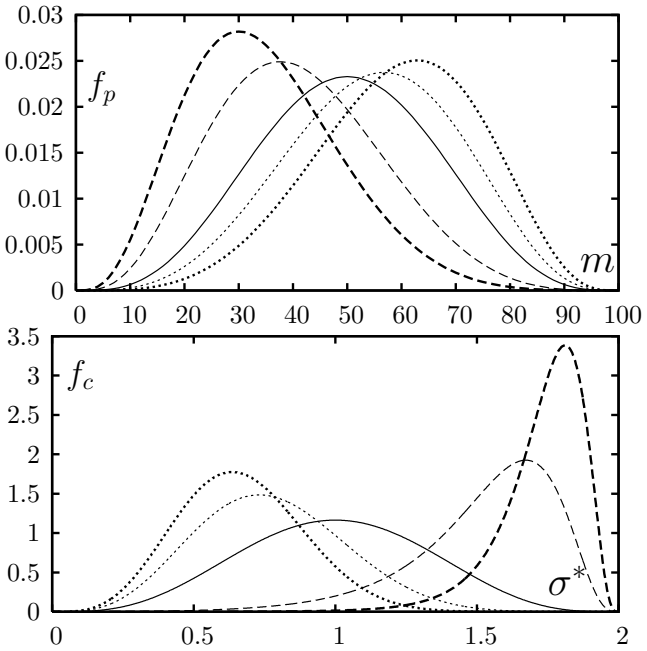

Figure 11. Polymer (top panel) and colloidal (bottom panel) distribution functions of the parent phase (solid lines), low-density shadow phase (dashed lines) and high-density shadow phase (dotted lines) at $P^* = 8$ calculated using BMCSL TPT (thick lines) and NGCS TPT (thin lines).

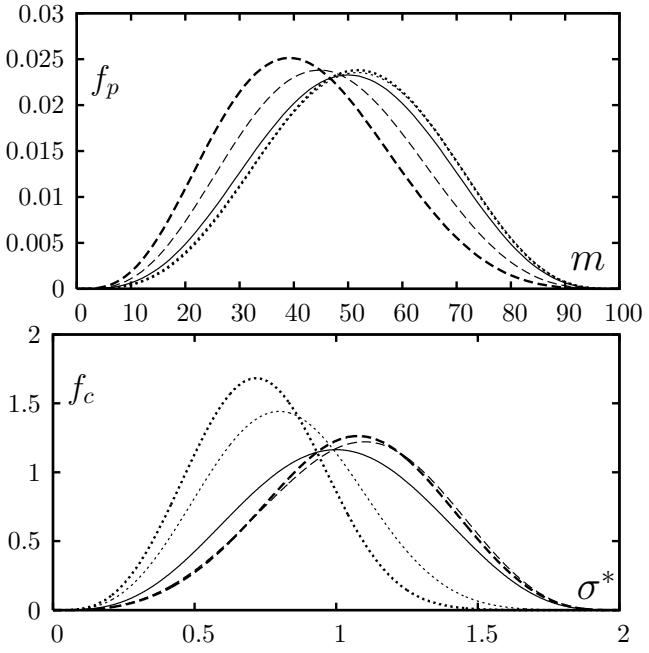

Figure 12. Polymer (top panel) and colloidal (bottom panel) distribution functions of the parent phase (solid lines), low-density branch of the critical binodal (dashed lines) and high-density branch of the critical binodal (dotted lines) at $P^* = 8$ calculated using BMCSL TPT (thick lines) and NGCS TPT (thin lines).